



This is a repository copy of *An extended isogeometric collocation method for fracture analysis*.

White Rose Research Online URL for this paper:

<https://eprints.whiterose.ac.uk/211665/>

Version: Published Version

Article:

Fathi, F., Oakley, J.E. orcid.org/0000-0002-9860-4093 and de Borst, R. (2024) An extended isogeometric collocation method for fracture analysis. *International Journal for Numerical Methods in Engineering*, 125 (16). e7507. ISSN 0029-5981

<https://doi.org/10.1002/nme.7507>

Reuse

This article is distributed under the terms of the Creative Commons Attribution (CC BY) licence. This licence allows you to distribute, remix, tweak, and build upon the work, even commercially, as long as you credit the authors for the original work. More information and the full terms of the licence here:

<https://creativecommons.org/licenses/>

Takedown

If you consider content in White Rose Research Online to be in breach of UK law, please notify us by emailing eprints@whiterose.ac.uk including the URL of the record and the reason for the withdrawal request.





eprints@whiterose.ac.uk
<https://eprints.whiterose.ac.uk/>

RESEARCH ARTICLE

WILEY

An extended isogeometric collocation method for fracture analysis

Farshid Fathi¹  | Jeremy E. Oakley² | René de Borst¹ 

¹Department of Civil and Structural Engineering, University of Sheffield, Sheffield, UK

²School of Mathematics and Statistics, University of Sheffield, Sheffield, UK

Correspondence

René de Borst, Department of Civil and Structural Engineering, University of Sheffield, Sheffield, S1 3JD, UK.

Email: r.deborst@sheffield.ac.uk

Funding information

EPSRC, Grant/Award Number: R/171264-11-1

Abstract

A collocation method is developed for discrete fracture models in the context of the partition-of-unity method. Spline technologies used in isogeometric analysis (IGA) are exploited to provide a smooth inter-element transition of gradients, thus allowing to get rid of extra flux terms at element boundaries which are generated by Lagrange polynomials. Bézier extraction is utilised to formulate IGA commensurate with a standard finite element data-structure. The efficacy of the proposed approach is examined through different numerical examples and is compared with other discrete methods for fracture analysis. The proposed approach is competitive in terms of accuracy with the least computational cost, rendering it a suitable candidate for superseding available collocation approaches for fracture simulation. Moreover, the approach naturally assesses the possibility of physics informed neural networks for fracture simulation, to which collocation is central.

KEYWORDS

collocation method, extended isogeometric analysis, Galerkin method, partition of unity

1 | INTRODUCTION

Computational mechanics, in particular finite element analysis (FEA),^{1,2} has played a pivotal role in providing simulation tools with an unprecedented accuracy. However, the presence of singularities, as occur for instance in fracture, still pose challenges. The importance, however, of accurate computational tools for fracture simulations is high, since experimental studies on fracture mechanisms are difficult to conduct and not always reliable. Therefore, there is much interest in developing numerical strategies for fracture analyses. Herein, we seek to develop an alternative method which directly exploits the partial differential equation (PDE), and is known as collocation.^{3,4}

From a variational viewpoint, collocation employs weighted residuals of the strong form that are enforced at some arbitrary evaluation points, that is, PDEs are used directly, different from the Galerkin method,¹ which transforms the governing PDEs into a weak format and provides the basis for standard FEA. A typical approach to derive a collocation method is to choose the Dirac- δ as the test function at evaluation points.^{3,5} An alternative approach evaluates the weighted residuals at particular locations where the chosen test functions return the Kronecker- δ property.⁴ This has been exploited in a so-called collocated FEA⁶ that uses Gauss-Lobatto Lagrange polynomials as test functions and Gauss-Lobatto points as collocation/evaluation points. The Kronecker- δ property of Gauss-Lobatto Lagrange bases at its quadrature points

This is an open access article under the terms of the [Creative Commons Attribution](https://creativecommons.org/licenses/by/4.0/) License, which permits use, distribution and reproduction in any medium, provided the original work is properly cited.

© 2024 The Authors. *International Journal for Numerical Methods in Engineering* published by John Wiley & Sons Ltd.

leads to an innate collocation method, and can be classified as a special form of the Petrov-Galerkin method.⁶ Collocation methods have been incorporated in a wide range of applications, from spectral elements^{3,4} to meshfree methods.⁷

More recently, IsoGeometric Analysis (IGA), a paradigm for explicitly utilising a geometric model in an analysis, has also been used in conjunction with collocation.⁸ IGA integrates computer aided design (CAD) and FEA tools and aims at mitigating the computational cost by bypassing mesh generation,^{9,10} since the model directly results from the CAD model. Indeed, the same spline functions are utilised as in the design packages, for example, Non-Uniform Rational B-Splines (NURBS),^{7,11} T-splines^{12,13} or Powell-Sabin B-splines.¹⁴

From a computational perspective, IGA tends to outperform standard FEA in a per-degree-of-freedom comparison on accuracy and robustness.^{15,16} The smooth nature of splines provides higher-order continuity even across element boundaries where C^0 -continuity is all that Lagrange polynomials can offer. This improves the evaluation of stresses and guarantees mass balance for fluid problems,^{17,18} and is particularly important when higher-order differentials have to be evaluated, as in for example, the Cahn–Hilliard equation.^{19,20} When using IGA together with collocation the advantages can even be more pronounced. Indeed, utilising the strong form of governing equations calls for a smooth set of basis functions even in an elasto-statics problem where the weak form is naturally consistent with the lowest continuity order, that is, C^0 . The presence of the inter-element continuity is imperative in the collocation method, as it allows for getting rid of extra flux terms at element boundaries.⁶

Theoretical aspects of blending IGA and collocation method were first investigated for an elliptic problem,²¹ followed by a variational interpretation of the method for static and dynamic cases.²² They were further explored in other applications, such as Bernoulli–Euler and Timoshenko beams, and Kirchhoff plate elements.^{23–25} In a comparison between Galerkin and collocation isogeometric analyses⁷ it was demonstrated that the latter can significantly reduce the computational cost and provides a guarantee against shear locking.^{24,25}

De Lorenzis et al.²⁶ have shown that there can be a significant loss of accuracy in case of a strong imposition of Neumann boundary conditions. As a remedy, they suggested a hybrid approach that adopts a Galerkin method to locally satisfy Neumann boundary conditions in a weak sense. This idea has been tested in the context of spectral collocation,²⁷ and has been further utilised in fracture analyses using phase-field models.²⁸ For pure collocation in IGA spurious oscillations can result for Neumann boundary conditions and near a crack.

Herein, we will combine collocation IGA with the partition of unity method (PUM) for a discrete representation of the crack. Unlike phase-field contributions,^{28,29} we extend the formulation by providing a local switch for cohesive tractions at the discontinuity. This is one of the advantages of discrete fracture over phase-field models, where cohesive fracture is not modelled naturally. The resulting approach enables assessing physics informed neural networks (PINNs)³⁰ in a discrete fracture analysis, where the collocation method plays a central role and will be the subject of future work. We explore fracture modelling using isogeometric collocation, resulting in an extended isogeometric collocation method, and adopt Dirac- δ as the test function for the collocation method.

The article is structured as follows. Section 2 presents the governing equations at the bulk and at the discontinuity. Next, the prerequisites are outlined for the extended isogeometric collocation method. This is followed by a succinct review of NURBS as basis functions adopted for IGA, Section 3. Section 4 discusses implementation aspects, including compatibility enforcement, enrichment and integration schemes. Finally, some case studies are presented which demonstrate the capability of the approach to model stationary and progressive fracturing.

2 | GOVERNING EQUATIONS

Rate-independent, isotropic linear elasticity has been utilised for the bulk material, and small displacement gradients are assumed throughout. It is noted that the term extended FEA is adopted to encompass a wider family, including extended isogeometric FEA.^{16,17,31–33} Where used, the eXtended Finite Element Method (XFEM) denotes extended FEA that adopts Lagrange polynomials as the set of basis functions.^{34–36} Therefore, we strictly avoid using these terms interchangeably.

The partition-of-unity method (PUM) allows for approximating the enrichment functions γ with the shape functions φ

$$\mathbf{u}_{\text{PUM}}^h = \sum_i \varphi_i(x) \left(\sum_j \mathbf{u}_{ij} \gamma_j(x) \right) \quad \text{where} \quad \sum_i \varphi_i(x) = 1. \quad (1)$$

Combining customary FEA and PUM leads to generalised finite element method (GFEM)³⁷ whose displacement field is decomposed into standard and enhanced sections, Equation (2)

$$\mathbf{u}^h = \mathbf{u}_{\text{std}}^h + \mathbf{u}_{\text{enh}}^h = \sum_i \varphi_i^{\text{std}}(x) \hat{\mathbf{u}}_i + \sum_i \varphi_i^{\text{enh}}(x) \left(\sum_j \tilde{\mathbf{u}}_{ij} \gamma_j(x) \right), \quad (2)$$

where \mathbf{u}^h denote the approximated displacements, $\hat{\mathbf{u}}$ and $\tilde{\mathbf{u}}$ are the standard and the enhanced displacements. The standard part governs the general boundary value problem estimated by the set of shape functions φ^{std} , and the enhanced part approximates the set of enrichment functions γ by means of basis functions φ^{enh} . The local support of φ^{enh} enables a local evaluation of γ , for instance a sharp gradient due to localisation.

To deal with cracks and voids, we adopt a Heaviside function $\mathcal{H}(x_n)$ for γ with approximants which are locally enriched in an extrinsic manner,³⁴ and the method is called extended FEA. x_n indicates the normal distance from crack. The displacement field \mathbf{u} for a cracked medium reads:

$$\mathbf{u}^h = \hat{\mathbf{u}}^h + \mathcal{H}_{\Gamma_d}(x_n) \tilde{\mathbf{u}}^h. \quad (3)$$

This approach has been widely used in XFEM^{34–36} and proven accurate, efficient and robust for fracture analysis. Later, it was incorporated in IGA context as eXtended IsoGeometric Analysis (XIGA).^{16,17,31–33}

Now, we aim at expanding XIGA to use collocation. Consider the body Ω in Figure 1. In the absence of the acceleration, the quasi-static total potential energy yields:

$$\Psi^{\text{pot}} = \mathcal{E}^{\text{int}} - \mathcal{P}^{\text{ext}} = \frac{1}{2} \int_{\Omega} \boldsymbol{\sigma}(u) : \boldsymbol{\epsilon}(u) \, d\Omega - \int_{\Gamma_t} \bar{\mathbf{t}} \cdot \mathbf{u} \, d\Gamma - \int_{\Omega} \bar{\mathbf{b}} \cdot \mathbf{u} \, d\Omega \quad (4)$$

with stresses, strains, prescribed tractions and body forces indicated by $\boldsymbol{\sigma}$ and $\boldsymbol{\epsilon}$, $\bar{\mathbf{t}}$ and $\bar{\mathbf{b}}$, respectively. Applying the principle of virtual work, as a set of virtual displacement $\delta \mathbf{u}$ into Equation (4), leads to:

$$\delta \Psi^{\text{pot}} = \int_{\Omega} \boldsymbol{\sigma}(u) : \delta \boldsymbol{\epsilon}(u) \, d\Omega - \int_{\Gamma_t} \bar{\mathbf{t}} \cdot \delta \mathbf{u} \, d\Gamma - \int_{\Omega} \bar{\mathbf{b}} \cdot \delta \mathbf{u} \, d\Omega = 0, \quad (5)$$

with the virtual displacements $\delta \mathbf{u} = \delta \hat{\mathbf{u}} + \mathcal{H}_{\Gamma_d}(x_n) \delta \tilde{\mathbf{u}}$. The constitutive relationship between stress-strain is given as:

$$\boldsymbol{\sigma}(u) = \mathbb{C} \boldsymbol{\epsilon}(u) = \mathbb{C} \boldsymbol{\nabla}^s \mathbf{u} \quad (6)$$

with $\boldsymbol{\nabla}^s$ the symmetric gradient operator and \mathbb{C} the elasticity matrix. Inserting Equation (6) into (5) gives:

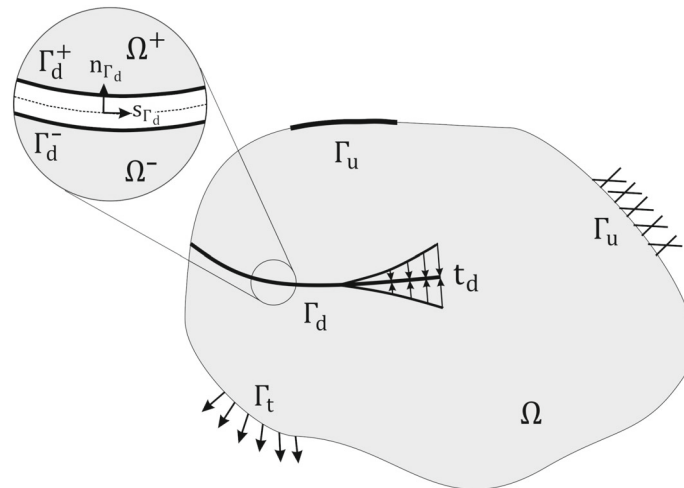


FIGURE 1 Boundary value problem Ω with the discontinuity Γ_d and cohesive tractions \mathbf{t}_d .

$$\begin{aligned} \delta\Psi^{\text{pot}} = & \int_{\Omega} \mathbb{C} \nabla^s \mathbf{u} : (\nabla^s \delta \hat{\mathbf{u}} + \mathcal{H}_{\Gamma_d}(x_n) \nabla^s \delta \tilde{\mathbf{u}} + 2\delta\Gamma_d(x_n) \text{sym}(\delta \tilde{\mathbf{u}} \otimes \mathbf{n}_{\Gamma_d})) \, d\Omega - \int_{\Gamma_t} \bar{\mathbf{t}} \cdot (\delta \hat{\mathbf{u}} + \mathcal{H}_{\Gamma_d}(x_n) \delta \tilde{\mathbf{u}}) \, d\Gamma \\ & - \int_{\Omega} \bar{\mathbf{b}} \cdot (\delta \hat{\mathbf{u}} + \mathcal{H}_{\Gamma_d}(x_n) \delta \tilde{\mathbf{u}}) \, d\Omega = 0. \end{aligned} \quad (7)$$

where \mathbf{n}_{\square} denotes the vector normal to the respective boundary \square and $\text{sym}(\bullet)$ indicates the symmetric value of (\bullet) . Utilising the identity $\int_{\Omega} \delta\Gamma_d(x_n) \phi(x) \, d\Omega = \int_{\Gamma_d} \phi(x) \, d\Gamma$ and further rewriting the ensuing term for Dirac- δ at the boundary Γ_d (discontinuity)

$$\int_{\Omega} \mathbb{C} \nabla^s \mathbf{u} : \delta\Gamma_d(x_n) \text{sym}(\delta \tilde{\mathbf{u}} \otimes \mathbf{n}_{\Gamma_d}) \, d\Omega = \int_{\Gamma_d} (\boldsymbol{\sigma} \cdot \mathbf{n}_{\Gamma_d}) \cdot \delta \tilde{\mathbf{u}} \, d\Gamma = \int_{\Gamma_d} \mathbf{t}_d \cdot \delta \tilde{\mathbf{u}} \, d\Gamma \quad (8)$$

leads to

$$\int_{\Omega} \mathbb{C} \nabla^s \mathbf{u} : \nabla^s \delta \hat{\mathbf{u}} \, d\Omega - \int_{\Gamma_t} \bar{\mathbf{t}} \cdot \delta \hat{\mathbf{u}} \, d\Gamma - \int_{\Omega} \bar{\mathbf{b}} \cdot \delta \hat{\mathbf{u}} \, d\Omega = 0, \quad (9a)$$

$$\int_{\Omega} \mathbb{C} \nabla^s \mathbf{u} : \mathcal{H}_{\Gamma_d}(x_n) \nabla^s \delta \tilde{\mathbf{u}} \, d\Omega + 2 \int_{\Gamma_d} \mathbf{t}_d \cdot \delta \tilde{\mathbf{u}} \, d\Gamma - \int_{\Gamma_t} \bar{\mathbf{t}} \cdot \mathcal{H}_{\Gamma_d}(x_n) \delta \tilde{\mathbf{u}} \, d\Gamma - \int_{\Omega} \bar{\mathbf{b}} \cdot \mathcal{H}_{\Gamma_d}(x_n) \delta \tilde{\mathbf{u}} \, d\Omega = 0 \quad (9b)$$

for continuous and discontinuous fields, respectively.

2.1 | Constitutive relation at the discontinuity

So far, the governing equations have been written in a general sense, where non-linear deformations and their gradients form a zone at the vicinity of the crack tip. The size of the fracture process zone determines the strategy for a fracture modelling that removes/retains \mathbf{t}_d at Γ_d . The latter leads to a general case with a non-zero size of the fracture process zone. We adopt the cohesive-zone model to account for the fracture process zone. The corresponding cohesive traction law \mathbf{t}_d reads:

$$\mathbf{t}_d([\mathbf{u}], \kappa) = \mathbf{Q}^T \cdot \mathbf{t}_d^{\text{loc}}([\mathbf{u}], \kappa), \quad (10)$$

where $[\mathbf{u}] = \sum_{k=1}^{n_{\text{enr}}} N_k \tilde{u}_k$ denotes the displacement jump and κ indicates a history parameter. $\mathbf{t}_d^{\text{loc}}$ are the tractions in the local coordinate system at the discontinuity, which are transferred into the global coordinate system through the rotation matrix \mathbf{Q} . The loading/unloading criterion is governed by a Kuhn–Tucker condition:

$$f = [\mathbf{u}_n] \text{ or } [\mathbf{u}_s] - \kappa \leq 0, \quad \dot{\kappa} \geq 0, \quad \dot{\kappa} f = 0. \quad (11)$$

Subscripts \circ_s and \circ_n denote the normal and tangential components of \circ , respectively.

3 | EXTENDED ISOGEOMETRIC COLLOCATION METHOD

The set of equations in (9) denote the conventional weak form utilised in extended FEA. For the formulation of the collocation method we first integrate by parts and then apply divergence theorem for at least C^1 -continuous approximants (such as NURBS) to derive

$$\int_{\Omega} \mathbb{C} \nabla^s \mathbf{u} : \nabla^s \delta \hat{\mathbf{u}} \, d\Omega = \int_{\Gamma_t} (\mathbb{C} \nabla^s \mathbf{u} \cdot \mathbf{n}_{\Gamma_t}) \cdot \delta \hat{\mathbf{u}} \, d\Gamma - \int_{\Omega} \text{div}(\mathbb{C} \nabla^s \mathbf{u}) \cdot \delta \hat{\mathbf{u}} \, d\Omega, \quad (12a)$$

$$\int_{\Omega} \mathbb{C} \nabla^s \mathbf{u} : \mathcal{H}_{\Gamma_d}(x_n) \nabla^s \delta \tilde{\mathbf{u}} \, d\Omega = \int_{\Gamma_t} (\mathbb{C} \nabla^s \mathbf{u} \cdot \mathbf{n}_{\Gamma_t}) \cdot \mathcal{H}_{\Gamma_d}(x_n) \delta \tilde{\mathbf{u}} \, d\Gamma - \int_{\Omega} \text{div}(\mathcal{H}_{\Gamma_d}(x_n) \mathbb{C} \nabla^s \mathbf{u}) \cdot \delta \tilde{\mathbf{u}} \, d\Omega, \quad (12b)$$

where by definition $\text{div}(\bullet) = \nabla^s \cdot \bullet$. The identity $\text{div}(\square \vec{\circ}) = \square \text{div}(\vec{\circ}) + \nabla \square \cdot \vec{\circ}$ can be utilised to further expand the last term in Equation (12b), where \square and $\vec{\circ}$ denote the scalar and vector fields, respectively.

$$\int_{\Omega} \operatorname{div}(\mathcal{H}_{\Gamma_d}(x_n) \mathbb{C} \nabla^s \mathbf{u}) \cdot \delta \tilde{\mathbf{u}} \, d\Omega = \int_{\Omega} \operatorname{div}(\mathbb{C} \nabla^s \mathbf{u}) \cdot \mathcal{H}_{\Gamma_d}(x_n) \delta \tilde{\mathbf{u}} \, d\Omega + 2 \int_{\Omega} \mathbb{C} \nabla^s \mathbf{u} \cdot \delta_{\Gamma_d}(x_n) \operatorname{sym}(\delta \tilde{\mathbf{u}} \otimes \mathbf{n}_{\Gamma_d}) \, d\Omega. \quad (13)$$

Recalling the identity $\int_{\Omega} \delta_{\Gamma_d}(x_n) \phi(x) \, d\Omega = \int_{\Gamma_d} \phi(x) \, d\Gamma$, the variational forms of the elasto-static problem built for collocation method read

$$- \int_{\Omega} \left(\operatorname{div}(\mathbb{C} \nabla^s \mathbf{u}) + \bar{\mathbf{b}} \right) \cdot \delta \hat{\mathbf{u}} \, d\Omega + \int_{\Gamma_t} \left(\mathbb{C} \nabla^s \mathbf{u} \cdot \mathbf{n}_{\Gamma_t} - \bar{\mathbf{t}} \right) \cdot \delta \hat{\mathbf{u}} \, d\Gamma = 0, \quad (14a)$$

$$- \int_{\Omega} \left(\operatorname{div}(\mathbb{C} \nabla^s \mathbf{u}) + \bar{\mathbf{b}} \right) \cdot \mathcal{H}_{\Gamma_d}(x_n) \delta \tilde{\mathbf{u}} \, d\Omega - 2 \int_{\Gamma_d} \left(\mathbb{C} \nabla^s \mathbf{u} \cdot \mathbf{n}_{\Gamma_d} - \mathbf{t}_d \right) \cdot \delta \tilde{\mathbf{u}} \, d\Gamma + \int_{\Gamma_t} \left(\mathbb{C} \nabla^s \mathbf{u} \cdot \mathbf{n}_{\Gamma_t} - \bar{\mathbf{t}} \right) \cdot \mathcal{H}_{\Gamma_d}(x_n) \delta \tilde{\mathbf{u}} \, d\Gamma = 0. \quad (14b)$$

It is noted that we could achieve identical results from an interface crack viewpoint, see Appendix A.

3.1 | Non-uniform rational B-splines

Herein, we adopt NURBS as weighted B-splines that are capable of accurately parametrising the geometry. A curve can be expressed as a linear combination of NURBS basis functions, that map a parametric coordinate ξ onto the physical domain:

$$\mathbf{C}(\xi) = \sum_{k=1}^{n_{\text{IGA}}} R_k(\xi) \mathbf{P}_k, \quad (15)$$

where n_{IGA} is the number of control points coordinates \mathbf{P} . Weights \mathbf{w} and the set of B-spline basis functions \mathbf{N} , defined recursively by the Cox-de Boor formula,² form the NURBS shape functions:

$$R_{k,p}(\xi) = \frac{w_k N_{k,p}}{W(\xi)}, \quad (16)$$

with $W(\xi) = \sum_{k=1}^n N_k(\xi) w_k$ and p denoting the order of the underlying knot vector. Bézier extraction has been adopted to provide an elementwise framework in compliance with standard finite element data-structures,^{38,39}

$$\mathbf{N}^e = \mathbf{C}^e \mathbf{B}. \quad (17)$$

\mathbf{C} is the Bézier extraction operator,³² and \mathbf{B} is the set of Bernstein polynomials defined on $[-1 \, 1]$,

$$B_{k,p}(\xi) = \frac{1}{2} (1 - \xi) B_{k,p-1}(\xi) + \frac{1}{2} (1 + \xi) B_{k-1,p-1}(\xi), \quad (18a)$$

$$B_{1,0}(\xi) \equiv 1, \quad (18b)$$

$$B_{k,p}(\xi) \equiv 0 \quad \text{if } k < 1 \quad \text{or} \quad k > p + 1, \quad (18c)$$

and

$$\mathbf{R}^e(\xi) = \mathbf{W}^e \mathbf{C}^e \frac{\mathbf{B}^e(\xi)}{W^e(\xi)}, \quad (19)$$

where \mathbf{W}^e is the diagonal matrix of weights. Generalisation to higher dimensions is possible via tensor products.

3.2 | Discretised equations

We discretise the weak forms commensurate with the finite element data-structure, so that the domain Ω is subdivided into non-overlapping smaller sections, called elements

$$\Omega = \bigcup_{e=1}^{n_{\text{elm}}} \Omega^e, \quad (20)$$

where n_{elm} denote the number of elements. We wish to explore different combinations of Galerkin and collocation methods in order to find the best combination for the extended isogeometric collocation method. As noted before, implementation of Neumann boundary conditions can give rise to the oscillatory response in some spatial discretisations. The local use of Galerkin method has been proven an effective remedy,²⁶ which we therefore employ at Neumann and other external boundaries.

In order to utilise Equation (2) in the extended isogeometric collocation method, test and weight functions have been chosen commensurate with the functionality of the proposed hybrid Galerkin-collocation method at different locations. Particularly, we use the sifting property of the Dirac- δ for the collocation points τ^{col} :

$$\int_{\Omega} \phi(x) \delta_{\text{Dirac}}(x - x^*) d\Omega = \phi(x^*) \quad \forall x^* \in \tau^{\text{col}}. \quad (21)$$

For internal boundaries such as cracks, the Heaviside function in the enhanced term violates the requirement of the sifting property that $\phi(x)$ is continuous. Therefore, we must use a Galerkin method at the vicinity of the crack. This is unlike phase-field representation of isogeometric collocation method where the discontinuity is approximated by a continuous exponential decay, so that the sifting property can be used. Yet, oscillations have been reported at the vicinity of the crack when collocation method is used near the crack.²⁸ Unsurprisingly, the Galerkin method mitigates the issue for a phase-field model.²⁸

Inserting NURBS basis functions for the Galerkin method that is used at external/internal boundaries yields

$$\begin{aligned} \delta \hat{\mathbf{u}}^h &= \sum_{i=1}^k R_i(x) \delta \hat{\mathbf{u}}_i + \sum_{i=k+1}^n \delta_{\text{Dirac}}(x - x_i^*) \delta \hat{\mathbf{u}}_i, & \hat{\mathbf{u}}^h &= \sum_{j=1}^n R_j(x) \hat{\mathbf{u}}_j, \\ \delta \tilde{\mathbf{u}}^h &= \sum_{i=1}^{n_{\text{enr}}} R_i(x) \delta \tilde{\mathbf{u}}_i, & \tilde{\mathbf{u}}^h &= \sum_{j=1}^{n_{\text{enr}}} R_j(x) \tilde{\mathbf{u}}_j. \end{aligned} \quad (22)$$

The external and the internal forces read:

$$\mathbf{f}_{\hat{\mathbf{u}}^*}^{\text{ext}} = \bigcup_{e=1}^{n_{\text{elm}}} \left[\int_{\Omega} \mathbf{R}^T(\mathbf{x}) \bar{\mathbf{b}}(\mathbf{x}) d\Omega + \bar{\mathbf{b}}(\mathbf{x}^*) \right]^e, \quad \mathbf{f}_{\tilde{\mathbf{u}}^*}^{\text{ext}} = \bigcup_{e=1}^{n_{\text{elm}}} \left[\int_{\Omega} (\mathbf{R}^{\text{enr}})^T(\mathbf{x}) \bar{\mathbf{b}}(\mathbf{x}) d\Omega \right]^e, \quad \begin{matrix} \mathbf{x}^* \in \tau^{\text{col}} \subset \Omega \\ \mathbf{x} \subset \Omega \end{matrix}, \quad (23a)$$

$$\mathbf{f}_{\hat{\mathbf{u}}}^{\text{ext}} = 0, \quad \mathbf{x} \subset \Gamma_d, \quad (23b)$$

$$\mathbf{f}_{\hat{\mathbf{u}}}^{\text{ext}} = \bigcup_{e=1}^{n_{\text{elm}}} \left[\int_{\Gamma_t} \mathbf{R}^T(\mathbf{x}) \bar{\mathbf{t}}(\mathbf{x}) d\Gamma + \bar{\mathbf{t}}(\mathbf{x}^*) \right]^e, \quad \mathbf{f}_{\tilde{\mathbf{u}}}^{\text{ext}} = \bigcup_{e=1}^{n_{\text{elm}}} \left[\int_{\Gamma_t} (\mathbf{R}^{\text{enr}})^T(\mathbf{x}) \bar{\mathbf{t}}(\mathbf{x}) d\Gamma \right]^e, \quad \begin{matrix} \mathbf{x}^* \in \tau^{\text{col}} \subset \Gamma_t \\ \mathbf{x} \subset \Gamma_t \end{matrix}, \quad (23c)$$

and

$$\mathbf{f}_{\hat{\mathbf{u}}}^{\text{int}} = \bigcup_{e=1}^{n_{\text{elm}}} \left[\int_{\Omega} \mathbf{R}^T(\mathbf{x}) \mathbb{H} \mathbf{R}(\mathbf{x}) \mathbf{u} d\Omega + \mathbb{H} \mathbf{R}(\mathbf{x}^*) \mathbf{u} \right]^e, \quad \mathbf{f}_{\tilde{\mathbf{u}}}^{\text{int}} = \bigcup_{e=1}^{n_{\text{elm}}} \left[\int_{\Omega} (\mathbf{R}^{\text{enr}})^T(\mathbf{x}) \mathbb{H} \mathbf{R}(\mathbf{x}) \mathbf{u} d\Omega \right]^e, \quad \begin{matrix} \mathbf{x}^* \in \tau^{\text{col}} \subset \Omega \\ \mathbf{x} \subset \Omega \end{matrix}, \quad (24a)$$

$$\mathbf{f}_{\hat{\mathbf{u}}}^{\text{int}} = \bigcup_{e=1}^{n_{\text{elm}}} \left[2 \int_{\Gamma_d} \left(\mathbf{R}^T(\mathbf{x}) \mathbb{n}_{\Gamma_d}^T \mathbb{D} \mathbf{R}(\mathbf{x}) \tilde{\mathbf{u}} - \mathbf{R}^T \mathbf{t}_d(\mathbf{x}) \right) d\Gamma \right]^e, \quad \mathbf{x} \subset \Gamma_d, \quad (24b)$$

$$\mathbf{f}_{\hat{\mathbf{u}}}^{\text{int}} = \bigcup_{e=1}^{n_{\text{elm}}} \left[\int_{\Gamma_t} \mathbf{R}^T \mathbb{n}_{\Gamma_d}^T \mathbb{D} \mathbf{R}(\mathbf{x}) \mathbf{u} d\Gamma + \mathbb{n}_{\Gamma_d}^T \mathbb{D} \mathbf{R}(\mathbf{x}^*) \mathbf{u} \right]^e, \quad \mathbf{f}_{\tilde{\mathbf{u}}}^{\text{int}} = \bigcup_{e=1}^{n_{\text{elm}}} \left[\int_{\Gamma_t} (\mathbf{R}^{\text{enr}})^T(\mathbf{x}) \mathbb{n}_{\Gamma_d}^T \mathbb{D} \mathbf{R}(\mathbf{x}^*) \mathbf{u} d\Gamma \right]^e, \quad \begin{matrix} \mathbf{x}^* \in \tau^{\text{col}} \subset \Gamma_t \\ \mathbf{x} \subset \Gamma_t \end{matrix}, \quad (24c)$$

where

$$\mathbb{n}_{\Gamma_d}^T = \begin{bmatrix} (n_{\Gamma_d})_x & 0 & (n_{\Gamma_d})_y \\ 0 & (n_{\Gamma_d})_y & (n_{\Gamma_d})_x \end{bmatrix}, \quad (25)$$

and

$$[\bullet]^{\text{enr}} = \mathcal{H}_{\Gamma_d}(\mathbf{x}) [\bullet]. \quad (26)$$

$\mathbb{D}\mathbf{R}$ and $\mathbb{H}\mathbf{R}$ indicate the first and the second derivative operators of basis functions.

The linearised discrete equations for a Newton–Raphson solver read:

$$\begin{bmatrix} \mathbf{K}_{\hat{u}\hat{u}}^{\Omega} + \mathbf{K}_{\hat{u}\hat{u}}^{\Gamma_t} & \mathbf{K}_{\hat{u}\hat{u}}^{\Omega} + \mathbf{K}_{\hat{u}\hat{u}}^{\Gamma_t} \\ \mathbf{K}_{\hat{u}\hat{u}}^{\Omega} + \mathbf{K}_{\hat{u}\hat{u}}^{\Gamma_t} & \mathbf{K}_{\hat{u}\hat{u}}^{\Omega} + \mathbf{K}_{\hat{u}\hat{u}}^{\Gamma_t} + \mathbf{K}_{\hat{u}\hat{u}}^{\Gamma_d} \end{bmatrix} \begin{bmatrix} \Delta \hat{\mathbf{u}} \\ \Delta \hat{\mathbf{u}} \end{bmatrix} = \begin{bmatrix} \mathbf{f}_{\hat{u}}^{\text{ext}} \\ \mathbf{f}_{\hat{u}}^{\text{ext}} \end{bmatrix} - \begin{bmatrix} \mathbf{f}_{\hat{u}}^{\text{int}} \\ \mathbf{f}_{\hat{u}}^{\text{int}} \end{bmatrix}. \quad (27)$$

It is noteworthy that the stiffness matrix is generally asymmetric,⁶ different from the more traditional extended FEA. Derivative operators and tangent terms of Equation (27) are given in the Appendix.

4 | IMPLEMENTATION ASPECTS

Compatibility enforcement, that is, localising the discontinuous enhanced terms in a narrow region around the crack path, is imperative in extended FEA. However, the support overlap of NURBS basis functions impedes a complete removal of the enhanced term at locations other than cracked elements. Nevertheless, compatibility enforcement narrows it down to a small region around the crack, reducing the error to a sufficiently narrow band, which can be further reduced with mesh refinement.¹⁶ Moreover, the higher-order continuity of NURBS (C^p $p > 0$) complicates the enrichment scheme during crack propagation. In this section, we discuss remedies and implementation aspects.

4.1 | Collocated evaluations and numerical integration

Motivated by previous studies on collocation IGA,^{21,22,26,28} we adopt Greville abscissae⁴⁰ that are constructed on a univariate knot vector of degree p :

$$x_I = \frac{\xi_{I+1} + \xi_{I+2} + \cdots + \xi_{I+p}}{p} \quad I = 1 \dots m, \quad (28)$$

where m is the number of basis functions. It is noted that in the context of IGA these points can play the role of collocation points as well.⁴¹ Greville points have a bijective relation with control points, that is, there is a one-to-one correspondence between Greville points and control points.

For extended FEA, however, the additional enhanced term is locally involved in approximating the solution within the cracked element. To properly represent the discontinuity in the cracked element, it is necessary that a sufficient number of quadrature points are provided at sections divided by the crack.³⁵ Therefore, regardless of the approximants, Lagrange polynomials³⁵ or NURBS,³² we use Gaussian quadrature for approximating the discontinuity. Hence, we adopt Greville points to evaluate the collocation method, and Gauss-quadrature where we switch to Galerkin method.

4.2 | Enrichment of individual points

Since the Galerkin method is adopted at the vicinity of the crack, as well as at external boundaries, we can identically use the enrichment strategy prescribed in XIGA.^{16,32} Hence, points at, or in front of the crack tip are not enriched. Disregarding this would lead to an incorrect solution for cohesive fracture when adopting relatively coarse meshes.³² The front is usually defined in either of two ways, by means of a tangential level-set³³ or the elementwise approach.^{16,32} These approaches lead to very similar results,¹⁷ at least for a small displacement gradient regime. Herein, we adopt an elementwise propagation.³²

We illustrate the enrichment strategy for quadratic and quartic NURBS in Figure 2. Collocation and Galerkin points are shown for standard and enhanced fields, separately. We consider two scenarios to find the best approach, namely: Hybrid Collocation-Galerkin approach (HCG), and HCG approach augmented with extra Galerkin in the standard field (HCXG). For comparison purposes a fully Galerkin method (GLK) is also considered. Figure 2 illustrates the enrichment scheme for HCG (A and B) and HCXG (C and D), while GLK enrichment is identical to that of HCXG with all Galerkin points in the standard field.

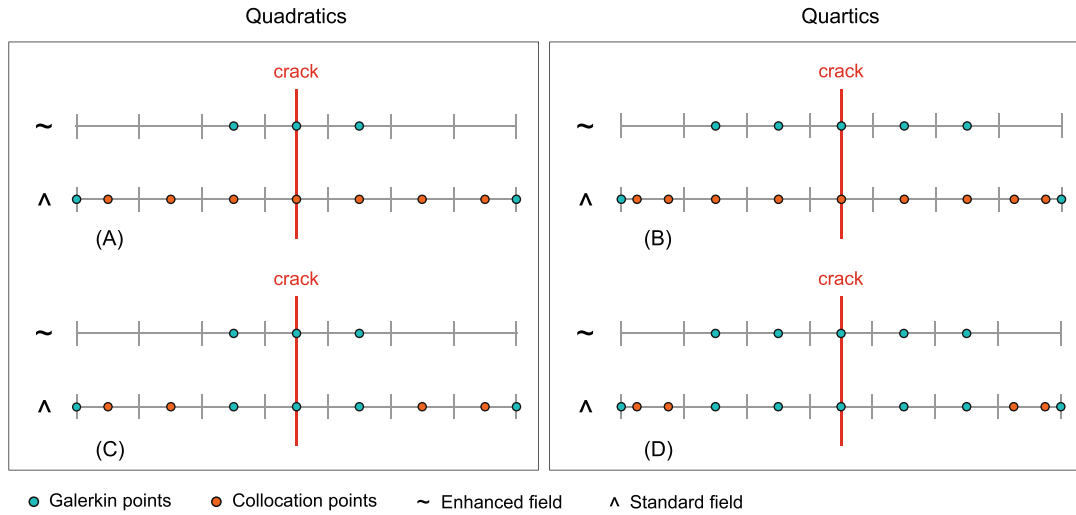


FIGURE 2 Quadratic and quartic NURBS enrichments illustrated for hybrid collocation-Galerkin (HCG) in A and B, and hybrid collocation-extra-Galerkin (HCXG) illustrated in C and D. The crack is located at the centre of a seven-element one-dimensional problem. For HCG, collocation is utilised at interior Greville points only, while Galerkin method is adopted at boundaries and for the enhanced field. In HCXG, however, the Galerkin method is also used for the interior points of the standard field, those corresponding to the points of the enhanced field.

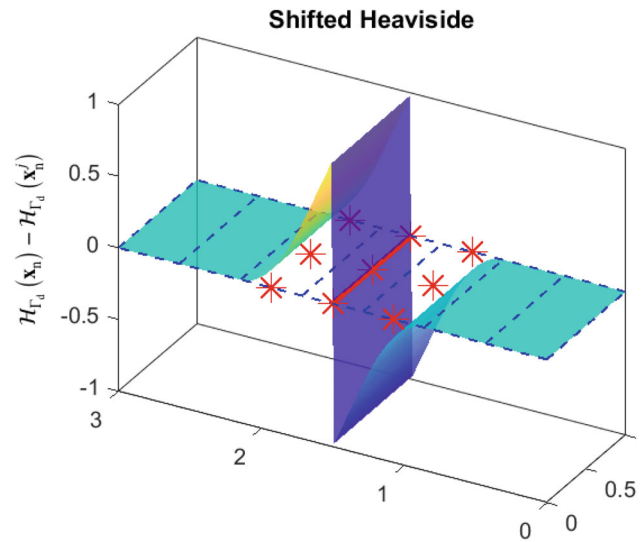


FIGURE 3 Shifting technique for a seven-element rectangular domain that is cracked at the centre. A quadratic NURBS is adopted here. The shifted Heaviside domain is extended to elements adjacent to the cracked. Yet, the domain is still narrower than natural support of enriched points. Enriched control points are indicated by red asterisks.

4.3 | Compatibility enforcement

In order to remove the undesired effect of the discontinuous (enhanced) field in front of the crack tip, we employ a blending technique by an extra Heaviside step function $H_{\Gamma_d}^{\text{Bl}}$. We adopt a shifting technique^{35,36} to localise the effect of the discontinuity normal to the crack path. This technique has been successfully tested for XIGA.^{32,33} While domain excess of the shifted Heaviside function from the cracked element is inevitable, shifting reduces the support of NURBS basis functions by confining the Heaviside term, as observed in Figure 3:

$$[\bullet]^{\text{enr}} = H_{\Gamma_d}^{\text{Bl}}(\mathbf{x}_s) \left(H_{\Gamma_d}(\mathbf{x}_n) - H_{\Gamma_d}(\mathbf{x}_n^j) \right) [\bullet]^j \quad j = 1 \dots n_{\text{enr}}^e, \quad (29)$$

where $\mathcal{H}_{\Gamma_d}^{\text{Bl}}(\mathbf{x}_s)$ denotes the blending function on the tangential distance of the integration point \mathbf{x}_s . n_{enr}^e is the number of enriched points of the element under consideration. The shifted Heaviside function reads $\mathcal{H}_{\Gamma_d}(\mathbf{x}_n) - \mathcal{H}_{\Gamma_d}(\mathbf{x}_n^j)$ which mitigates the domain excess of the enhanced term normal to the crack path.^{32,33} \mathbf{x}_n^j is the normal distance of j th enriched control point of the element. The extent of the shifted domain (i.e., the enriched field) depends on the continuity-order of the NURBS utilised; for instance, 3 elements for quadratic and cubic, and 5 elements for quartic and quintic NURBS.³² Finally, Equation (26) is substituted for Equation (29). It is noteworthy that a simple shifting technique successfully confines the enhanced terms to the cracked element within XFEM due to the C^0 -continuity of Lagrange polynomials across element boundaries.

4.4 | Direction of crack extension

While IGA improves the stress distribution in general, the local oscillations of stresses around the crack tip cannot be completely avoided. This is important for progressing fractures, where the crack extension is determined by the state of the stress at the crack tip. This calls for a smoothing scheme to better evaluate the crack propagation criterion. Here, we adopt a non-local approach⁴² in the form of a Gaussian weight function similar to what utilised in XIGA.³² The propagation criterion compares the equivalent traction with the fracture strength at the extension direction. Crack nucleation occurs upon satisfying this criterion at certain number of evaluation points along the extension path.

5 | NUMERICAL EXAMPLES AND DISCUSSION

We assess the efficacy of the formulation under a wide range of examples. Mode-I fracture is assumed throughout this section. Note that we only examine quadratic ($p = 2$) and quartic ($p = 4$) NURBS due to the fact that even polynomial-degrees return $\mathcal{O}(p)$ while odd polynomial-degrees lead to $\mathcal{O}(p - 1)$ rate of convergence based on H^1 semi-norm error.^{21,22,28} By definition, L^2 norm and H^1 semi-norm errors read:

$$e_{L^2} = \left(\int_{\Omega} (\mathbf{u}^h - \mathbf{u}_{\text{exct}})^2 d\Omega \right)^{\frac{1}{2}} \quad e_{H^1} = \left(\int_{\Omega} \left(\frac{\partial \mathbf{u}^h}{\partial \mathbf{x}} - \frac{\partial \mathbf{u}_{\text{exct}}}{\partial \mathbf{x}} \right)^2 d\Omega \right)^{\frac{1}{2}}. \quad (30)$$

5.1 | One-dimensional bar

We first assess the formulations for a one-dimensional problem, namely a bar subjected to a sinusoidal load, see Figure 4. Since there are only Dirichlet boundary conditions for this problem, the comparison is between a pure collocation and a fully Galerkin method.

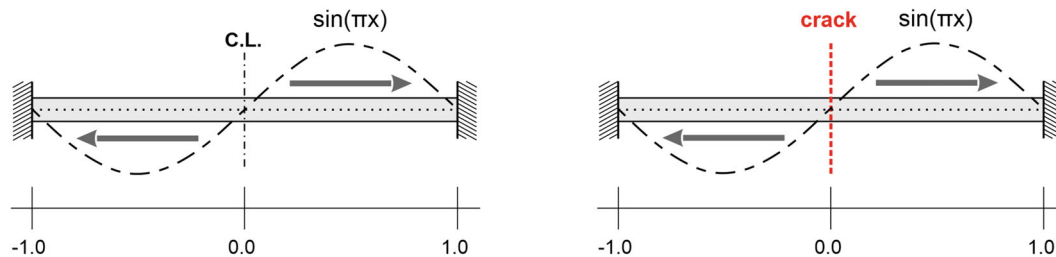


FIGURE 4 One dimensional (left) intact bar and (right) cracked bar subjected to sinusoidal load.

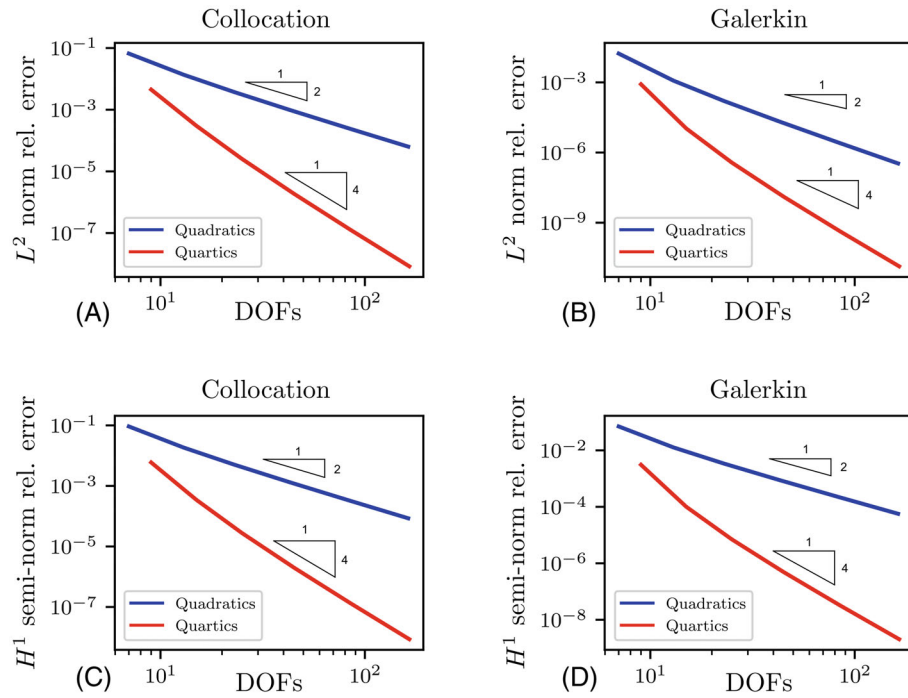


FIGURE 5 Comparison between pure collocation and fully Galerkin methods for an intact bar. Quadratic and quartic NURBS have been examined for L^2 norm (A and B) and H^1 semi-norm (C and D) errors.

5.1.1 | Intact bar

We first examine an undamaged bar in Figure 4 with Young's modulus $E = 1$ and the cross-section area $A = 1$. The exact solution reads:

$$u_{\text{exct}} = \frac{1}{\pi^2} \sin(\pi x), \quad \sigma_{\text{exct}} = \frac{1}{\pi} \cos(\pi x). \quad (31)$$

Figure 5 shows the L^2 norm and H^1 semi-norm errors for quadratic and quartic NURBS for pure collocation and for a fully Galerkin method, respectively. As expected, the Galerkin method leads to lower per-degree-of-freedom errors, at the cost of a higher computational cost in comparison with collocation methods. Owing to the discrete fracture model adopted in this article, even the smallest values for degrees of freedom (DOFs) lead to results within accepted error range, while much bigger values of DOFs has been reported for phase-field models²⁸ due to the smeared nature of the approach.

5.1.2 | Fractured bar

Now we place a traction-free crack at the middle of the bar, see Figure 4. A comparison between the proposed hybrid approaches, HCG and HCXG, and the fully Galerkin approach (GLK) is now made. Evaluations are done for the L^2 norm and H^1 semi-norm errors.

Figure 6 gives the comparison between HCG and HCXG (Figure 6A,C). For quadratic functions, the performances are close except for the very beginning of HCXG for L^2 norm error. This part of the graph corresponds to very few DOFs and, consequently, a response dominated by Galerkin section of the hybrid approach. This is confirmed by Figure 6B,D, where the blue curves intersect at the very beginning, that is, the fully Galerkin method (GLK) matches with HCXG. For quartic functions (red curves in Figure 6A,C), however, there is an obvious difference at the end of the red curves, where HCXG outperforms HCG. In a comparison between quadratic and quartic functions it is evident that quartic functions return smaller errors for both HCG and HCXG, with an exception for the beginning of L^2 norm, where the red and the blue curves intersect. A similar behaviour is observed for GLK (solid lines in Figure 6B). Next, we compare GLK and

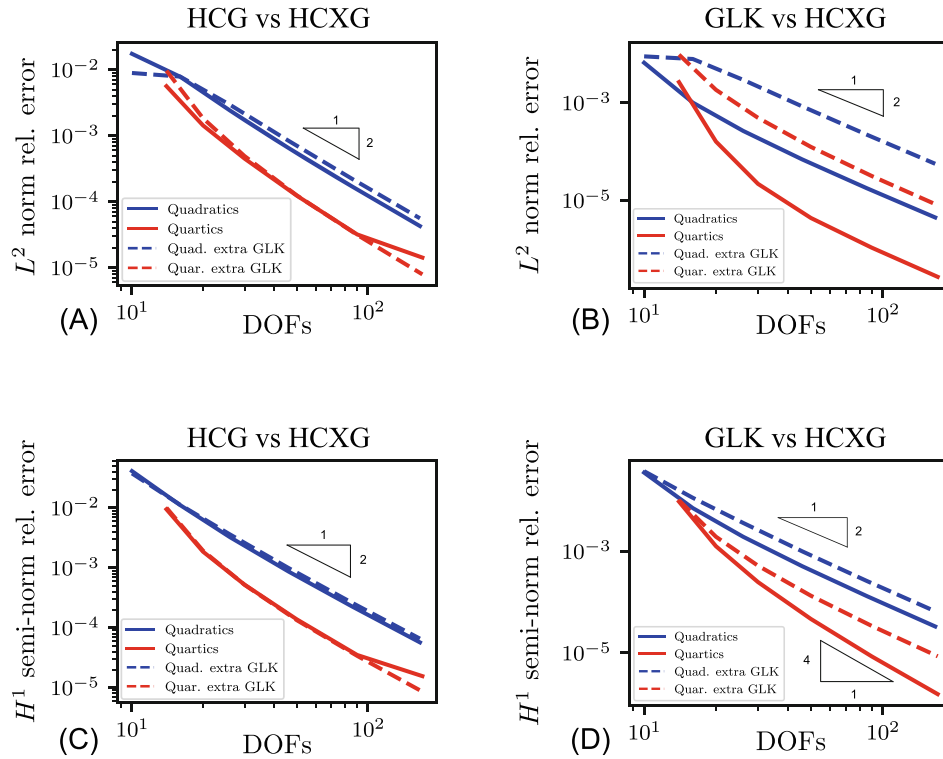


FIGURE 6 L^2 norm and H^1 semi-norm errors illustrated for hybrid collocation-Galerkin (HCG), hybrid collocation-extra-Galerkin (HCGXG) and Galerkin (GLK) approaches. Quadratic and quartic NURBS have been examined.

HCGXG in Figure 6B,D. As expected GLK exhibits a lower error in the L^2 norm and H^1 semi-norms at the expense of higher computational cost. The cost is a crucial issue when moving to higher dimensions, or to fine discretisations necessary to properly model crack propagation. We observe that HCGXG quadratic NURBS returns a convergence slope smaller than 4, which holds for GLK.

The overall displacements \mathbf{u} and their constituents, $\hat{\mathbf{u}}$ and $\tilde{\mathbf{u}}$, are shown in Figures 7 and 8, respectively. A good agreement is observed between HCG, HCGXG and GLK, while differences are more significant for the error representations, Figure 6. The stresses are another good measure of the differences between the approaches, as illustrated in Figure 9 for 11 and 21 elements. The results for quartic functions show an excellent agreement between the approaches for both discretisations, but those for quadratic functions are slightly poorer for 11 elements near the boundaries.

So far, we have examined all the possibilities of a blend between collocation and Galerkin methods. We now continue with fully Galerkin (GLK) and hybrid collocation-extra-Galerkin (HCGXG) approaches. Especially since evaluating cohesive terms for collocation, particularly Equation (24b), necessitates that some collocation points are located at the crack path. Abiding to this requirement implies an order reduction in isogeometric analysis⁴³ which is equivalent to changing the discretisation to accommodate the crack path, for example, interface element approach.^{44–46} This is, however, in contrast with the nature of PUM that decouples crack path from the underlying discretisation. Therefore, adopting a Galerkin form for the cracked element in both the standard and the enhanced field, as in the HCGXG approach, removes such a complication. Finally, HCGXG is closer to the idea that different orders for the standard and the enhanced terms must be avoided for XIGA.^{31,32} The only exception is blending IGA with local maximum entropy (LME)³³ for the standard and the enhanced fields, respectively, since the C^∞ -continuity of LME provides a flexibility that matches any NURBS order.³³

5.2 | Two-dimensional uniform tension test

The cohesive-zone model is now applied to a uniform tension test, see Figure 10. The crack is located at the centre of the plate and displacements are uniformly applied at the top and the bottom edges in opposite directions. The material

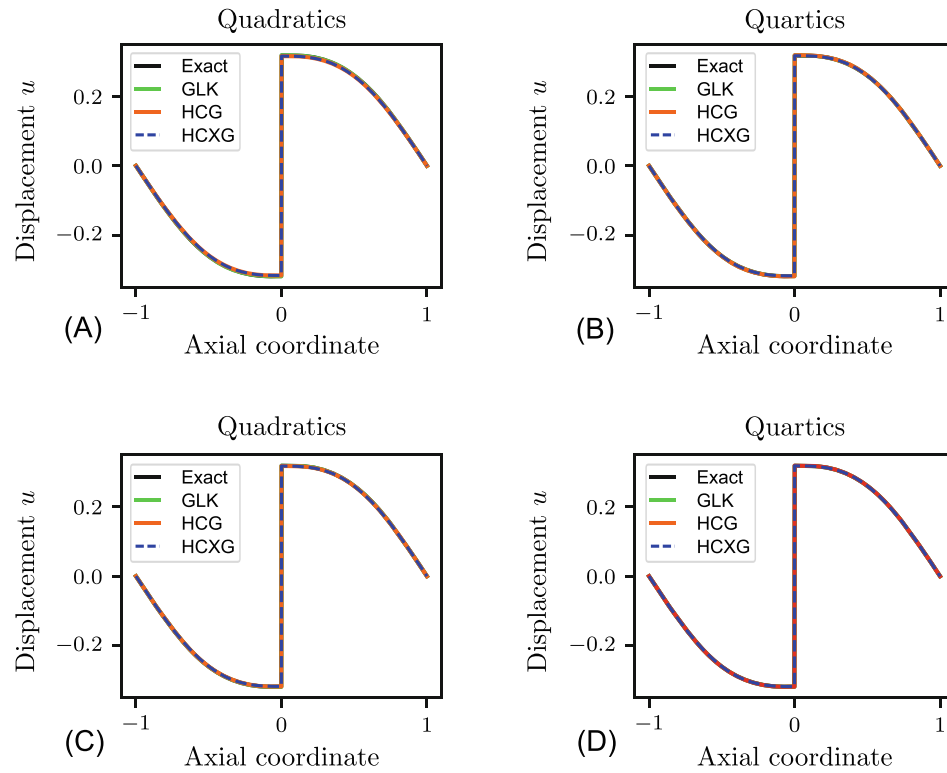


FIGURE 7 Displacement comparison for Galerkin (GLK), hybrid collocation-Galerkin (HCG) and hybrid collocation-extra-Galerkin (HCXG). Discretisations of 11 (A and B) and 21 elements (C and D) are illustrated.

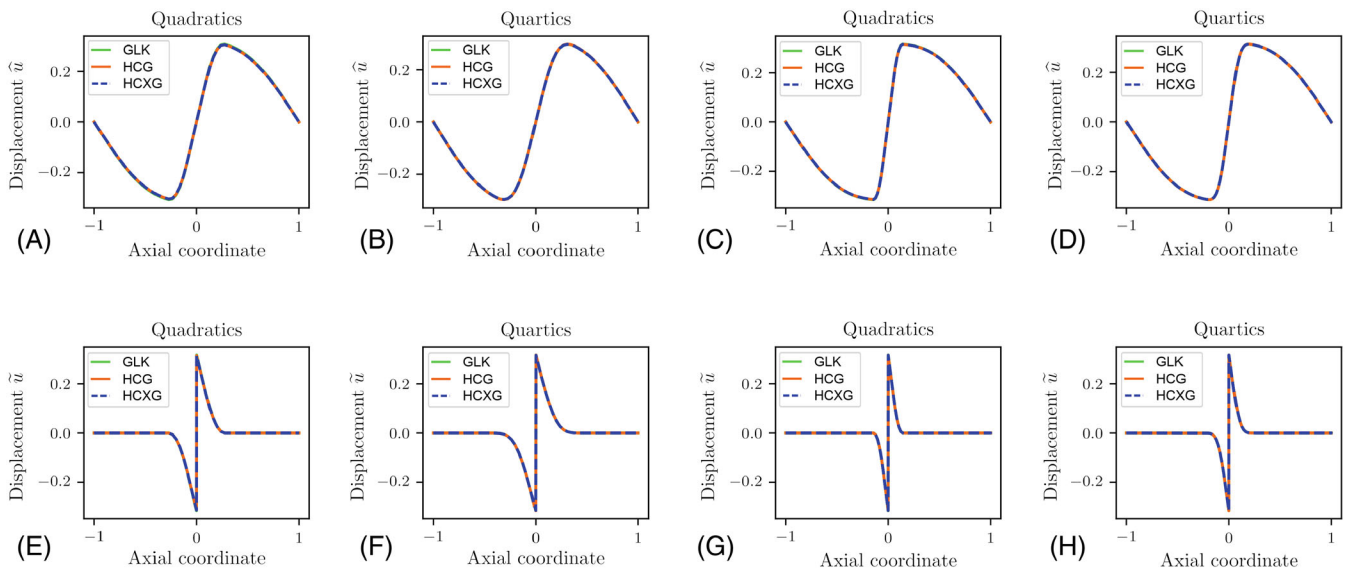


FIGURE 8 Displacements of the standard and the enhanced fields are compared for GLK, HCG and HCXG. Discretisations of 11 (A, B, E, and F) and 21 elements (C, D, G, and H) are illustrated.

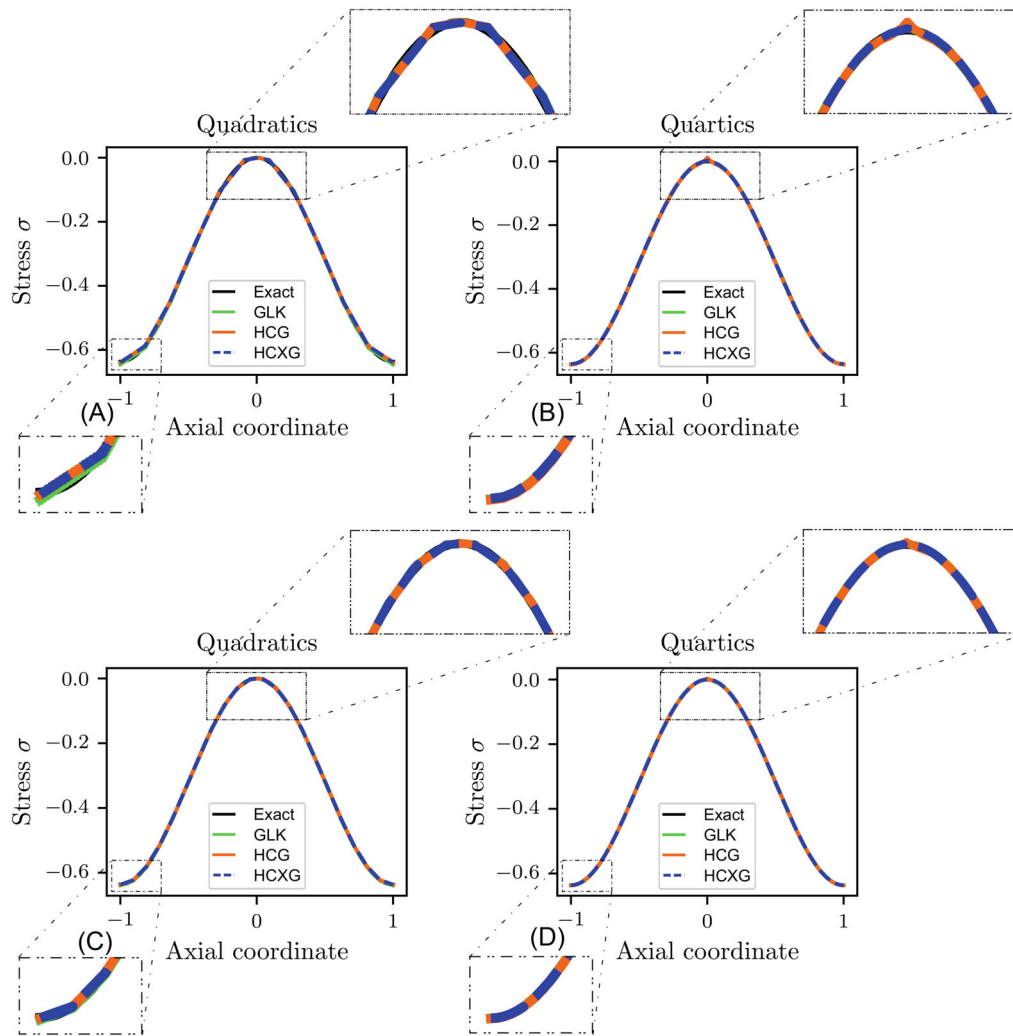


FIGURE 9 Stress comparison for Galerkin (GLK), hybrid collocation-Galerkin (HCG) and hybrid collocation-extra-Galerkin (HCXG). Results for discretisations of 11 (A and B) and 21 elements (C and D), respectively.

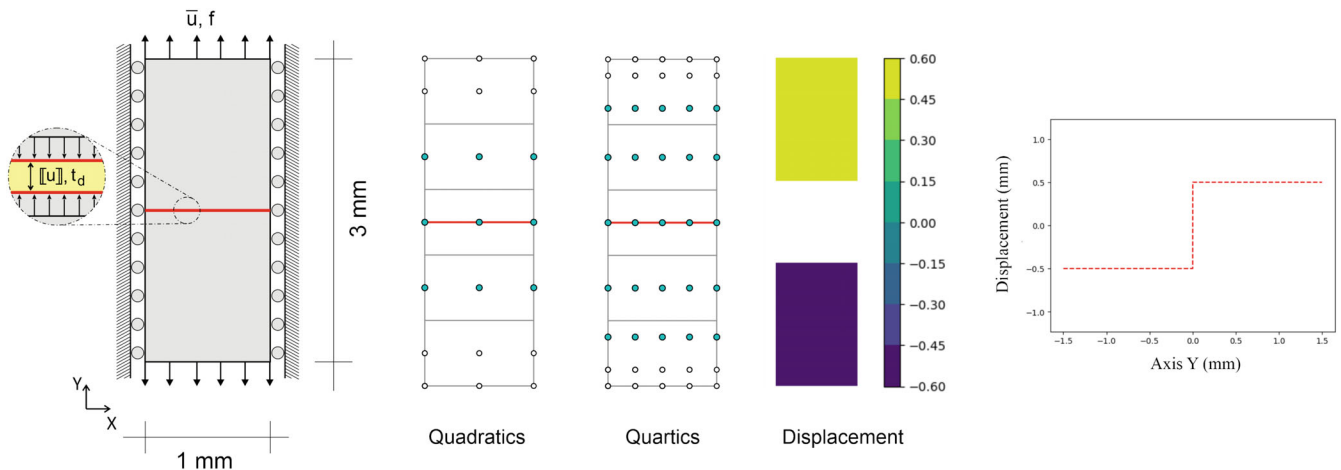


FIGURE 10 Cohesive fracture assessed in a uniform tension test. The enriched points (denoted in green) are illustrated for quadratic and quartic NURBS. Displacement contour and graph are also presented confirming the uniform opening and deformation at the presence of the non-zero Poisson's ratio. $\bar{\mathbf{u}}$, $[[\mathbf{u}]]$, \mathbf{f} , \mathbf{t}_d denote prescribed displacement, displacement jump, force and cohesive traction, respectively.

properties read: Young's modulus $E = 100$ MPa; Poisson's ratio $\nu = 0.3$; fracture strength $t_u = 1$ MPa; fracture energy $G_f = 0.1$ N/mm. The objective is to assess the evaluation of the governing equations in the presence of a non-zero Poisson's ratio and the integral terms at boundaries that are absent in standard FEA (see Γ_i integral terms in Equation (14)). Uniform opening and deformation similar to those in a one-dimensional problem are shown in Figure 10 which visually confirms the correct implementation. Quantitative assessments are made through two relative error measures. For an elastic material the behaviour of the structure can be related to the traction-opening relationship at the crack location as follows:

$$\text{Relative error 1} = \frac{||2 \int f d\bar{u} - \int t_d d[[u]]||}{||\int t_d d[[u]]||} \times 100.$$

The factor 2 denotes that the jump at the discontinuity is twice the displacement at the loading boundaries. The fracture energy also correlates with the behaviour of the structure:

$$\text{Relative error 2} = \frac{||2 \int f d\bar{u} - G_f||}{G_f} \times 100.$$

This is a more strict criterion as it compares the numerical results with an absolute value of an input.

An exponential decay is adopted for the traction-opening relationship at the discontinuity

$$t_d^{\text{loc}} = t_u \exp\left(-\frac{t_u}{G_f} \kappa\right). \quad (32)$$

Two discretisations (5 and 21 elements, respectively) are examined. The results for quadratic and quartic NURBS have been plotted in Figure 11 and the errors have been presented in Table 1 for a better comparison. For the coarse mesh, GLK and XICM perform poorly for quadratic NURBS (errors $> 10\%$), while quartic NURBS slightly improves the results (errors $\approx 7\%$ – 8%). For the fine mesh, however, GLK and XICM yield good results (errors $\leq 2\%$). For the more strict criterion, that is, relative error 2, XICM equals or exceeds GLK, with computational cost less than those of GLK or XIGA.

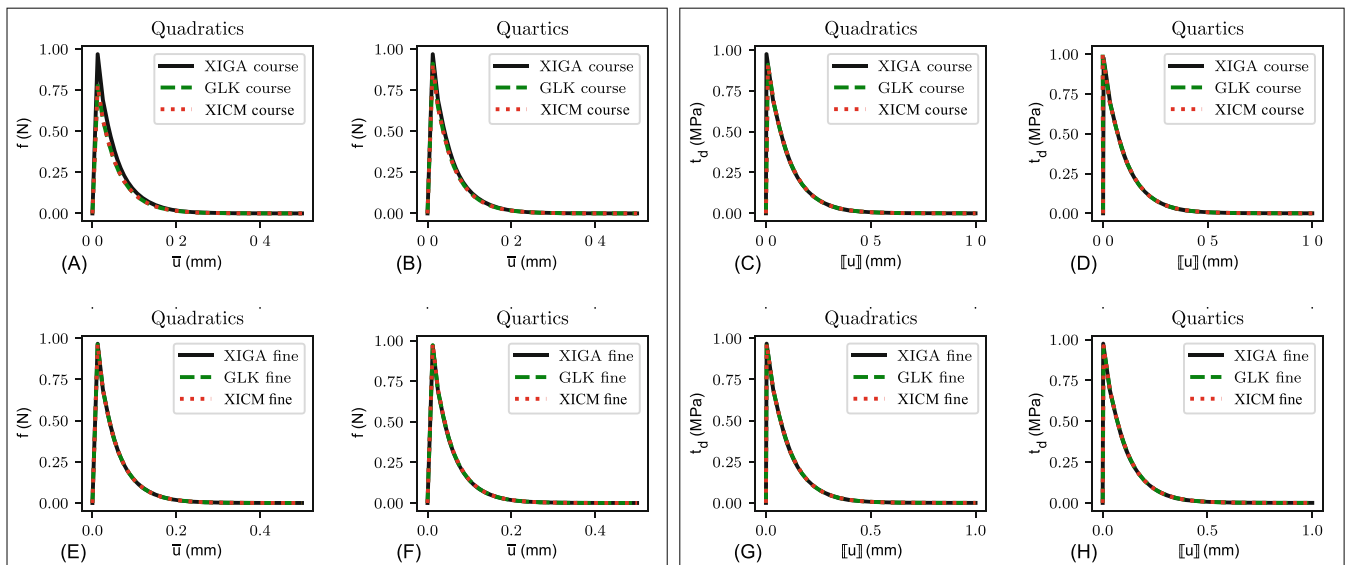


FIGURE 11 Exponential cohesive law for uniform tension test. Force-displacement and traction-opening graphs are shown in left and right hand side boxes, respectively. Extended isogeometric analysis (XIGA), Galerkin (GLK) and extended isogeometric collocation method (XICM) are compared for quadratic and quartic NURBS. Two discretisations have been examined, coarse (5 elements) and fine (21 elements) meshes.

TABLE 1 Comparison of released energy: Galerkin (GLK), extended isogeometric collocation method (XICM) and extended isogeometric analysis (XIGA) for an exponential traction-opening relation.

NURBS	Value/relative error	Coarse mesh			Fine mesh		
		GLK	XICM	XIGA	GLK	XICM	XIGA
Quadratics	Value (N mm ⁻¹)	0.0813	0.0813	0.0984	0.0979	0.0979	0.0983
	Rel. error 1 (%)	14.8	14.9	0.3	0.3	0.3	0.0
	Rel. error 2 (%)	18.7	18.7	1.6	2.1	2.1	1.7
Quartics	Value (N mm ⁻¹)	0.0922	0.0922	0.0984	0.0988	0.0996	0.0984
	Rel. error 1 (%)	8.1	8.1	0.3	1.0	1.6	0.3
	Rel. error 2 (%)	7.8	7.8	1.6	1.2	0.4	1.6

Note: Computations are done for coarse (5 elements) and fine (21 elements) discretisations.

5.3 | Fracturing: Single edge notched test

An assessment for a case with crack propagation completes the numerical investigations. A single-edge notched specimen is considered, see Figure 12. The geometry is discretised with 1740 (60 × 29) elements and quartic NURBS are adopted. The Greville abscissae are drawn in orange while the Galerkin method is evaluated at the green points, see Figure 12B. An exponential decay is adopted for the cohesive zone modelling at the crack location, and the material properties read: Young's modulus $E = 210$ GPa; Poisson's ratio $\nu = 0.3$; fracture strength $t_u = 2.5$ GPa; fracture energy $G_f = 2.7$ N/mm. The prescribed displacements at the top are applied incrementally:

$$\begin{cases} \Delta \bar{\mathbf{u}} = 5.625 \times 10^{-4} & \text{if } \bar{\mathbf{u}} \leq 4.5 \times 10^{-3} \\ \Delta \bar{\mathbf{u}} = 8.333 \times 10^{-5} & \text{if } \bar{\mathbf{u}} > 4.5 \times 10^{-3}. \end{cases}$$

The Galerkin method is adopted at all external boundaries regardless of the type. A full Galerkin method (GLK) will not be examined in this example as it is computationally more expensive than XIGA due to the integral terms at boundaries that are absent in a customary weak form. Hence, XICM is compared with XIGA by quantifying errors with respect to the energy dissipated by fracturing. The mechanical response of the structure is shown in Figure 12C. Despite slight differences at the peaks, similar patterns are observed for XICM and XIGA. To quantify the differences, the energy dissipated for fracturing is evaluated by computing the area below the structural behaviour, that is, force-displacement curve in Figure 12C, and is compared with $G_f \times l_{\text{crk}}$ where l_{crk} denotes the crack-path length. Errors of 3% and 1.3% result for XIGA and XICM, showing that XICM is competitive with respect to other approaches. Displacements and stress values are reported in Figure 12D. Finally, it is recalled that the comparison is made between two naturally different approaches, a collocation method corrected with Galerkin at certain locations (XICM) and a standard finite element Galerkin method (XIGA). Yet, the errors of the two approaches remain close.

It is worth comparing the computational cost between XICM and XIGA by correlating the cost for the assembly of each approach with the number of evaluation points, similar to the isogeometric collocation for phase-field fracture models.²⁸ We used $(p+1) \times (p+1)$ Gauss points for XIGA, resulting in a symmetric stiffness matrix. On the other hand, forming the asymmetric stiffness matrix for XICM requires consideration of both integration and collocation points, given its hybrid nature. We adopted $(p+1) \times (p+1)$ Gauss points for Galerkin method used in XICM, for instance at the boundaries and the vicinity of the crack, and collocated XICM is evaluated at collocation points only. The total number of evaluation points for XIGA is 43,500, while only 9432 points are used for XICM, representing a reduction of approximately 78% in the number of evaluation points with XICM. It is noted that the comparison pertains to the initial configuration of the problem, as the use of Galerkin method extends with the crack propagation.

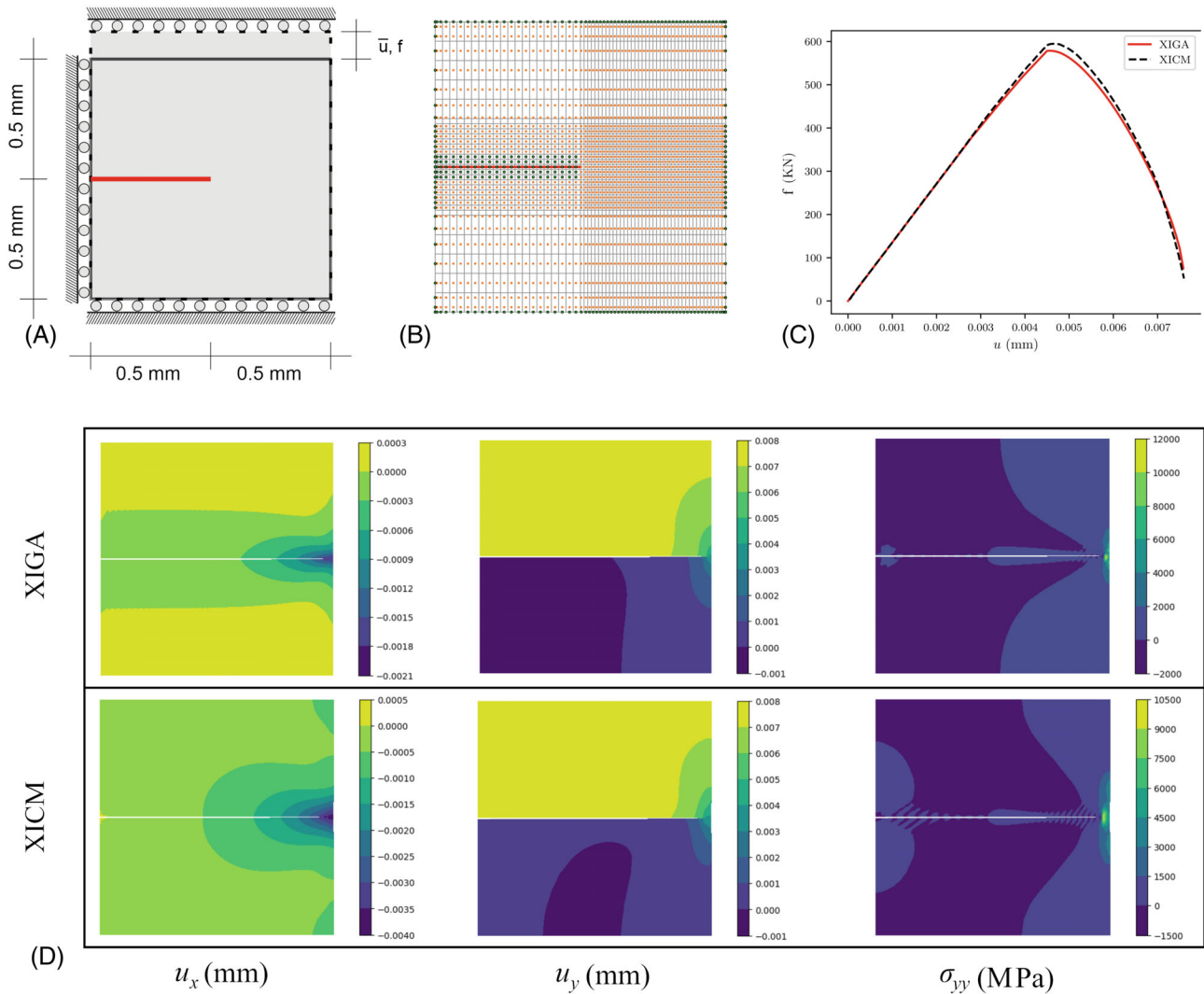


FIGURE 12 Single-edge notched specimen under tension test. The geometry and the special discretisation are shown in A and B, respectively. Orange points denote Greville abscissae for collocation method, and green ones indicate control points that Galerkin method is utilised for. The force-displacement response is illustrated in C while the displacements in \mathcal{X} - and \mathcal{Y} -directions along with the normal stresses in \mathcal{Y} -direction, which correspond to the last values reported for each approach in the force-displacement curve, are presented in D.

6 | CONCLUDING REMARKS

Collocation has been cast in the format of a partition-of-unity method for fracture analysis. Isogeometric analysis, using NURBS, has been adopted to handle the higher-order derivatives present in the strong form. In this article, the variational weak forms have been cast in the strong form by means of the Dirac- δ function. However, the discontinuous Heaviside function utilised for the discrete fracture model violates the requirement that the integrand of the Dirac- δ term is continuous. Local use of Galerkin method in the vicinity of the crack, as well as at Neumann boundary conditions, has been successful in stabilising the solution. The present approach compares favourably with respect to phase-field models as (i) it better supports coarse meshes due to the discrete nature, (ii) it leads to a lower computational cost owing to coarser discretisations, and (iii) it handles cohesive-zone models naturally. Additional techniques have been adopted to render the discontinuous enhanced term compatible with the standard field, that is, shifting and blending.

A range of examples has been investigated in this article. First, a bar subjected to a sinusoidal load has been examined with and without a crack. The former compares a pure collocation with a fully Galerkin method (GLK). For the cracked bar, however, a pure collocation is invalid since the sifting property of the Dirac- δ is only valid for continuous integrands, while the Heaviside function violates this. Therefore, a Galerkin method is exploited locally to remedy deficiencies of

the collocation method, for example, at cracks and at Neumann boundaries. Next, we have examined adding cohesive tractions to the crack in a two-dimensional uniform tension test. Finally, crack propagation has been modelled and the performance of XICM versus XIGA has been assessed. The numerical tests show that XICM is competitive with respect to other approaches for fracture analysis.

An important application for XICM are PINNs, to which collocation is central. Since PINNs use pure collocation, local amendments must be considered to enable discrete fracture simulation. Alternatively, moving to weak forms, some variants of PINNs can also resolve the issue. For instance, variational- and variational energy-PINNs are candidates for simulating fracture propagation with deep learning techniques.

ACKNOWLEDGMENTS

F. Fathi acknowledges the financial support from EPSRC (Grant R/171264-11-1).

DATA AVAILABILITY STATEMENT

Data sharing is not applicable to this article since no data sets were generated or analysed during this study.

ORCID

Farshid Fathi  <https://orcid.org/0000-0003-0789-3203>

René de Borst  <https://orcid.org/0000-0002-3457-3574>

REFERENCES

1. Hughes TJR. *The Finite Element Method: Linear Static and Dynamic Finite Element Analysis*. Courier Corporation; 2012.
2. de Borst R, Crisfield MA, Remmers JJC, Verhoosel CV. *Nonlinear Finite Element Analysis of Solids and Structures*. John Wiley & Sons; 2012.
3. van de Vosse FN, Minev PD. Spectral element methods: theory and applications. EUT Report. Eindhoven University of Technology; 1996.
4. Quarteroni A, Valli A. *Numerical Approximation of Partial Differential Equations*. Springer Science & Business Media; 2008.
5. Lapidus L, Pinder GF. *Numerical Solution of Partial Differential Equations in Science and Engineering*. John Wiley & Sons; 2011.
6. Schillinger D, Evans JA, Frischmann F, Hiemstra RR, Hsu MC, Hughes TJR. A collocated C0 finite element method: reduced quadrature perspective, cost comparison with standard finite elements, and explicit structural dynamics. *Int J Numer Methods Eng*. 2015;102:576-631.
7. Schillinger D, Evans JA, Reali A, Scott MA, Hughes TJR. Isogeometric collocation: cost comparison with Galerkin methods and extension to adaptive hierarchical NURBS discretizations. *Comput Methods Appl Mech Eng*. 2013;267:170-232.
8. Fahrenndorf F, De Lorenzis L. The isogeometric collocated contact surface approach. *Comput Mech*. 2022;70:785-802.
9. Hughes TJR, Cottrell JA, Bazilevs Y. Isogeometric analysis: CAD, finite elements, NURBS, exact geometry and mesh refinement. *Comput Methods Appl Mech Eng*. 2005;194:4135-4195.
10. Kagan P, Fischer A, Bar-Yoseph PZ. New B-spline finite element approach for geometrical design and mechanical analysis. *Int J Numer Methods Eng*. 1998;41:435-458.
11. Chen L, Lingen FJ, de Borst R. Adaptive hierarchical refinement of NURBS in cohesive fracture analysis. *Int J Numer Methods Eng*. 2017;112:2151-2173.
12. Chen L, Verhoosel CV, de Borst R. Discrete fracture analysis using locally refined T-splines. *Int J Numer Methods Eng*. 2018;116:117-140.
13. Hageman T, de Borst R. Unequal order T-spline meshes for fracture in poroelastic media. *J Mech*. 2021;37:669-679.
14. Chen L, de Borst R. Cohesive fracture analysis using Powell-Sabin B-splines. *Int J Numer Anal Methods Geomech*. 2019;43:625-640.
15. Evans JA, Bazilevs Y, Babuška I, Hughes TJR. n -Widths, sup-infs, and optimality ratios for the k -version of the isogeometric finite element method. *Comput Methods Appl Mech Eng*. 2009;198:1726-1741.
16. Fathi F, de Borst R. Geometrically nonlinear extended isogeometric analysis for cohesive fracture with applications to delamination in composites. *Finite Elem Anal Des*. 2021;191:103527.
17. Fathi F, Chen L, Hageman T, de Borst R. Extended isogeometric analysis of a progressively fracturing fluid-saturated porous medium. *Int J Numer Methods Eng*. 2022;123:1861-1881.
18. Chen L, Fathi F, de Borst R. Hydraulic fracturing analysis in fluid-saturated porous medium. *Int J Numer Anal Methods Geomech*. 2022;46:3200-3216.
19. Gomez H, Calo VM, Bazilevs Y, Hughes TJR. Isogeometric analysis of the Cahn–Hilliard phase-field model. *Comput Methods Appl Mech Eng*. 2008;197:4333-4352.
20. Kästner M, Metsch P, de Borst R. Isogeometric analysis of the Cahn–Hilliard equation—a convergence study. *J Comput Phys*. 2016;305:360-371.
21. Auricchio F, Beirao da Veiga L, Hughes TJR, Reali A, Sangalli G. Isogeometric collocation methods. *Math Models Methods Appl Sci*. 2010;20:2075-2107.
22. Auricchio F, Beirao da Veiga L, Hughes TJR, Reali A, Sangalli G. Isogeometric collocation for elastostatics and explicit dynamics. *Comput Methods Appl Mech Eng*. 2012;249:2-14.
23. Reali A, Gomez H. An isogeometric collocation approach for Bernoulli–Euler beams and Kirchhoff plates. *Comput Methods Appl Mech Eng*. 2015;284:623-636.

24. Beirao da Veiga L, Lovadina C, Reali A. Avoiding shear locking for the Timoshenko beam problem via isogeometric collocation methods. *Comput Methods Appl Mech Eng*. 2012;241:38-51.
25. Auricchio F, Beirao da Veiga L, Kiendl J, Lovadina C, Reali A. Locking-free isogeometric collocation methods for spatial Timoshenko rods. *Comput Methods Appl Mech Eng*. 2013;263:113-126.
26. De Lorenzis L, Evans JA, Hughes TJR, Reali A. Isogeometric collocation: Neumann boundary conditions and contact. *Comput Methods Appl Mech Eng*. 2015;284:21-54.
27. Canuto C, Hussaini MY, Quarteroni A, Zang TA. *Spectral Methods: Fundamentals in Single Domains*. Springer Science & Business Media; 2007.
28. Schillinger D, Borden MJ, Stolarski HK. Isogeometric collocation for phase-field fracture models. *Comput Methods Appl Mech Eng*. 2015;284:583-610.
29. Gomez H, Reali A, Sangalli G. Accurate, efficient, and (iso) geometrically flexible collocation methods for phase-field models. *J Comput Phys*. 2014;262:153-171.
30. Raissi M, Perdikaris P, Karniadakis GE. Physics-informed neural networks: a deep learning framework for solving forward and inverse problems involving nonlinear partial differential equations. *J Comput Phys*. 2019;378:686-707.
31. De Luycker E, Benson DJ, Belytschko T, Bazilevs Y, Hsu MC. X-FEM in isogeometric analysis for linear fracture mechanics. *Int J Numer Methods Eng*. 2011;87:541-565.
32. Fathi F, Chen L, de Borst R. Extended isogeometric analysis for cohesive fracture. *Int J Numer Methods Eng*. 2020;121:4584-4613.
33. Fathi F, Chen L, de Borst R. X-IGALME: isogeometric analysis extended with local maximum entropy for fracture analysis. *Int J Numer Methods Eng*. 2021;122:6103-6125.
34. Fries TP, Belytschko T. The extended/generalized finite element method: an overview of the method and its applications. *Int J Numer Methods Eng*. 2010;84:253-304.
35. Khoei AR. *Extended Finite Element Method: Theory and Applications*. John Wiley & Sons; 2014.
36. Mohammadi S. *Extended Finite Element Method: for Fracture Analysis of Structures*. John Wiley & Sons; 2008.
37. Strouboulis T, Babuška I, Copps K. The design and analysis of the generalized finite element method. *Comput Methods Appl Mech Eng*. 2000;181:43-69.
38. Borden MJ, Scott MA, Evans JA, Hughes TJR. Isogeometric finite element data structures based on Bézier extraction of NURBS. *Int J Numer Methods Eng*. 2011;87:15-47.
39. de Borst R, Chen L. The role of Bézier extraction in adaptive isogeometric analysis: local refinement and hierarchical refinement. *Int J Numer Methods Eng*. 2018;113:999-1019.
40. Gordon WJ, Riesenfeld RF. B-spline curves and surfaces. *Computer Aided Geometric Design*. Academic Press; 1974:95-126.
41. Zou Z, Hughes TJR, Scott MA, Sauer RA, Savitha EJ. Galerkin formulations of isogeometric shell analysis: alleviating locking with Greville quadratures and higher-order elements. *Comput Methods Appl Mech Eng*. 2021;380:113757.
42. Jirásek M. Nonlocal damage mechanics. *Rev Eur Génie Civ*. 2007;11:993-1021.
43. Verhoosel CV, Scott MA, de Borst R, Hughes TJR. An isogeometric approach to cohesive zone modeling. *Int J Numer Methods Eng*. 2011;87:336-360.
44. Schellekens JCJ, de Borst R. On the numerical integration of interface elements. *Int J Numer Methods Eng*. 1993;36:43-66.
45. Segura JM, Carol I. On zero-thickness interface elements for diffusion problems. *Int J Numer Anal Methods Geomech*. 2004;28:947-962.
46. Irzal F, Remmers JJC, Verhoosel CV, de Borst R. An isogeometric analysis Bézier interface element for mechanical and poromechanical fracture problems. *Int J Numer Methods Eng*. 2014;97:608-628.

How to cite this article: Fathi F, Oakley JE, de Borst R. An extended isogeometric collocation method for fracture analysis. *Int J Numer Methods Eng*. 2024;e7507. doi: 10.1002/nme.7507

APPENDIX A. ANOTHER DERIVATION OF EXTENDED ISOGEOMETRIC COLLOCATION FORMULA

We can also derive Equations (14a) and (14b) by considering the discontinuity as an interface crack. First, we focus on the internal forces in weak forms, the first terms in Equations (9a) and (9b). Integrating by part

$$\int_{\Omega} \mathbb{C} \nabla^s \mathbf{u} : \nabla^s \delta \hat{\mathbf{u}} \, d\Omega = \int_{\Omega} \text{div}(\mathbb{C} \nabla^s \mathbf{u} \cdot \delta \hat{\mathbf{u}}) \, d\Omega - \int_{\Omega} \text{div}(\mathbb{C} \nabla^s \mathbf{u}) \cdot \delta \hat{\mathbf{u}} \, d\Omega, \quad (\text{A1a})$$

$$\int_{\Omega} \mathbb{C} \nabla^s \mathbf{u} : \mathcal{H}_{\Gamma_d}(x_n) \nabla^s \delta \tilde{\mathbf{u}} \, d\Omega = \int_{\Omega} \text{div}(\mathbb{C} \nabla^s \mathbf{u} \cdot \mathcal{H}_{\Gamma_d}(x_n) \delta \tilde{\mathbf{u}}) \, d\Omega - \int_{\Omega} \text{div}(\mathcal{H}_{\Gamma_d}(x_n) \mathbb{C} \nabla^s \mathbf{u}) \cdot \delta \tilde{\mathbf{u}} \, d\Omega. \quad (\text{A1b})$$

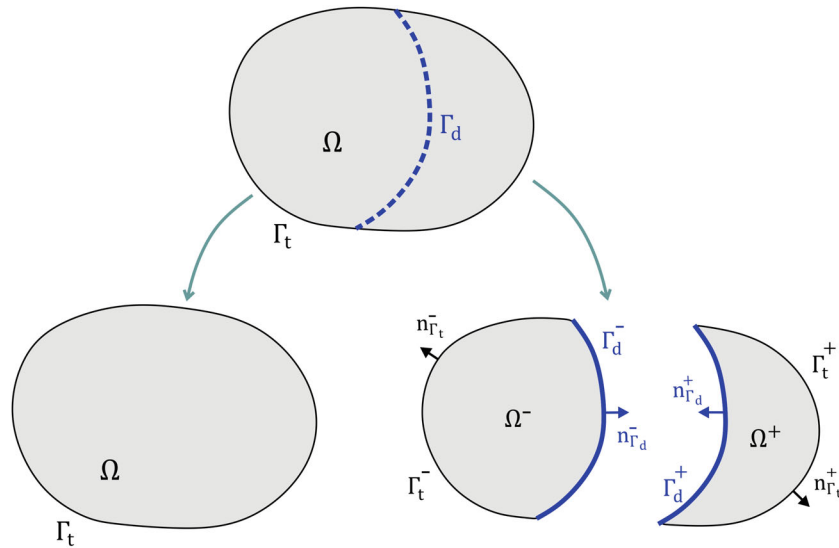


FIGURE A1 Divergence theorem in the context of PUM. The original problem is decoupled into continuous and discontinuous parts, which is in line with the decomposition of governing equations.

Applying the divergence theorem to the first term of the right-hand side in Equation (A1a) and adding external terms of the continuous problem yields:

$$-\int_{\Omega} \left(\text{div}(\mathbb{C} \nabla^s \mathbf{u}) + \bar{\mathbf{b}} \right) \cdot \delta \hat{\mathbf{u}} \, d\Omega + \int_{\Gamma_t} \left(\mathbb{C} \nabla^s \mathbf{u} \cdot \mathbf{n}_{\Gamma_t} - \bar{\mathbf{t}} \right) \cdot \delta \hat{\mathbf{u}} \, d\Gamma = 0. \quad (\text{A2})$$

For the discontinuous problem in Equation (A1b), we divide the object into two separate bodies $\Omega = \Omega^- + \Omega^+$, $\Gamma_t = \Gamma_t^- + \Gamma_t^+$ and $\Gamma_d = \Gamma_d^- + \Gamma_d^+$, see Figure A1. Next, we apply the divergence theorem on each body

$$\int_{\Omega^-} \text{div}(\mathbb{C} \nabla^s \mathbf{u} \cdot \mathcal{H}_{\Gamma_d}(x_n) \delta \tilde{\mathbf{u}}) \, d\Omega = \int_{\Gamma_t^-} (\mathbb{C} \nabla^s \mathbf{u} \cdot \mathcal{H}_{\Gamma_d}(x_n) \delta \tilde{\mathbf{u}}) \cdot \mathbf{n}_{\Gamma_t^-} \, d\Gamma + \int_{\Gamma_d^-} (\mathbb{C} \nabla^s \mathbf{u} \cdot \mathcal{H}_{\Gamma_d^-}(x_n) \delta \tilde{\mathbf{u}}) \cdot \mathbf{n}_{\Gamma_d^-} \, d\Gamma \quad (\text{A3})$$

and

$$\int_{\Omega^+} \text{div}(\mathbb{C} \nabla^s \mathbf{u} \cdot \mathcal{H}_{\Gamma_d}(x_n) \delta \tilde{\mathbf{u}}) \, d\Omega = \int_{\Gamma_t^+} (\mathbb{C} \nabla^s \mathbf{u} \cdot \mathcal{H}_{\Gamma_d}(x_n) \delta \tilde{\mathbf{u}}) \cdot \mathbf{n}_{\Gamma_t^+} \, d\Gamma + \int_{\Gamma_d^+} (\mathbb{C} \nabla^s \mathbf{u} \cdot \mathcal{H}_{\Gamma_d^+}(x_n) \delta \tilde{\mathbf{u}}) \cdot \mathbf{n}_{\Gamma_d^+} \, d\Gamma. \quad (\text{A4})$$

Adding Equations (A3) and (A4) and setting $\mathbf{n}_{\Gamma_d} = \mathbf{n}_{\Gamma_d^-} = -\mathbf{n}_{\Gamma_d^+}$ and $\mathcal{H}_{\Gamma_d^+} = -\mathcal{H}_{\Gamma_d^-} = 1$ yields

$$\int_{\Omega} \text{div}(\mathbb{C} \nabla^s \mathbf{u} \cdot \mathcal{H}_{\Gamma_d}(x_n) \delta \tilde{\mathbf{u}}) \, d\Omega = \int_{\Gamma_t} (\mathbb{C} \nabla^s \mathbf{u} \cdot \mathcal{H}_{\Gamma_d}(x_n) \delta \tilde{\mathbf{u}}) \cdot \mathbf{n}_{\Gamma_t} \, d\Gamma - 2 \int_{\Gamma_d} (\mathbb{C} \nabla^s \mathbf{u} \cdot \delta \tilde{\mathbf{u}}) \cdot \mathbf{n}_{\Gamma_d} \, d\Gamma. \quad (\text{A5})$$

By adding external terms of the discontinuous problem,

$$-\int_{\Omega} \left(\text{div}(\mathbb{C} \nabla^s \mathbf{u}) + \bar{\mathbf{b}} \right) \cdot \mathcal{H}_{\Gamma_d}(x_n) \delta \tilde{\mathbf{u}} \, d\Omega - 2 \int_{\Gamma_d} (\mathbb{C} \nabla^s \mathbf{u} \cdot \mathbf{n}_{\Gamma_d} - \mathbf{t}_d) \cdot \delta \tilde{\mathbf{u}} \, d\Gamma + \int_{\Gamma_t} \left(\mathbb{C} \nabla^s \mathbf{u} \cdot \mathbf{n}_{\Gamma_t} - \bar{\mathbf{t}} \right) \cdot \mathcal{H}_{\Gamma_d}(x_n) \delta \tilde{\mathbf{u}} \, d\Gamma = 0, \quad (\text{A6})$$

results.

Newly derived Equations (A2) and (A6) are identical to those in Equations (14a) and (14b).

APPENDIX B. DERIVATIVE OPERATORS

Differential operators used in this article are defined as follows:

$$\mathbb{D}\mathbf{R}(\mathbf{x}^*) = \begin{bmatrix} \mathbb{C}_{11} \frac{\partial \mathbf{R}_j}{\partial x} + \mathbb{C}_{13} \frac{\partial \mathbf{R}_j}{\partial y} & \mathbb{C}_{12} \frac{\partial \mathbf{R}_j}{\partial y} + \mathbb{C}_{13} \frac{\partial \mathbf{R}_j}{\partial x} \\ \mathbb{C}_{21} \frac{\partial \mathbf{R}_j}{\partial x} + \mathbb{C}_{23} \frac{\partial \mathbf{R}_j}{\partial y} & \mathbb{C}_{22} \frac{\partial \mathbf{R}_j}{\partial y} + \mathbb{C}_{23} \frac{\partial \mathbf{R}_j}{\partial x} \\ \mathbb{C}_{31} \frac{\partial \mathbf{R}_j}{\partial x} + \mathbb{C}_{33} \frac{\partial \mathbf{R}_j}{\partial y} & \mathbb{C}_{32} \frac{\partial \mathbf{R}_j}{\partial y} + \mathbb{C}_{33} \frac{\partial \mathbf{R}_j}{\partial x} \end{bmatrix}, \quad (\text{B1})$$

$$\mathbb{H}\mathbf{R}(\mathbf{x}^*) = \begin{bmatrix} \mathbb{C}_{11} \frac{\partial^2 \mathbf{R}_j}{\partial x^2} + \mathbb{C}_{31} \frac{\partial^2 \mathbf{R}_j}{\partial y \partial x} + \mathbb{C}_{13} \frac{\partial^2 \mathbf{R}_j}{\partial x \partial y} + \mathbb{C}_{33} \frac{\partial^2 \mathbf{R}_j}{\partial y^2} & \mathbb{C}_{12} \frac{\partial^2 \mathbf{R}_j}{\partial x \partial y} + \mathbb{C}_{32} \frac{\partial^2 \mathbf{R}_j}{\partial y^2} + \mathbb{C}_{13} \frac{\partial^2 \mathbf{R}_j}{\partial x^2} + \mathbb{C}_{33} \frac{\partial^2 \mathbf{R}_j}{\partial y \partial x} \\ \mathbb{C}_{21} \frac{\partial^2 \mathbf{R}_j}{\partial y \partial x} + \mathbb{C}_{31} \frac{\partial^2 \mathbf{R}_j}{\partial x^2} + \mathbb{C}_{23} \frac{\partial^2 \mathbf{R}_j}{\partial y^2} + \mathbb{C}_{33} \frac{\partial^2 \mathbf{R}_j}{\partial x \partial y} & \mathbb{C}_{22} \frac{\partial^2 \mathbf{R}_j}{\partial y^2} + \mathbb{C}_{32} \frac{\partial^2 \mathbf{R}_j}{\partial x \partial y} + \mathbb{C}_{23} \frac{\partial^2 \mathbf{R}_j}{\partial y \partial x} + \mathbb{C}_{33} \frac{\partial^2 \mathbf{R}_j}{\partial x^2} \end{bmatrix}. \quad (\text{B2})$$

APPENDIX C. TANGENTIAL STIFFNESS MATRICES

The linearised tangential stiffness matrix reads

$$\mathbf{K}_{\hat{u}\hat{u}}^{\Omega} = \frac{\partial \mathbf{f}_{\hat{u}}^{\text{int}}}{\partial \hat{\mathbf{u}}} = \bigcup_{e=1}^{n_{\text{elm}}} \left[\int_{\Omega} \mathbf{R}^T(\mathbf{x}) \mathbb{H}\mathbf{R}(\mathbf{x}) \, d\Omega + \mathbb{H}\mathbf{R}(\mathbf{x}^*) \right]^e, \quad (\text{C1a})$$

$$\mathbf{K}_{\hat{u}\hat{u}}^{\Omega} = \frac{\partial \mathbf{f}_{\hat{u}}^{\text{int}}}{\partial \hat{\mathbf{u}}} = \bigcup_{e=1}^{n_{\text{elm}}} \left[\int_{\Omega} \mathbf{R}^T(\mathbf{x}) \mathbb{H}\mathbf{R}^{\text{enr}}(\mathbf{x}) \, d\Omega \right]^e, \quad (\text{C1b})$$

$$\mathbf{K}_{\hat{u}\hat{u}}^{\Omega} = \frac{\partial \mathbf{f}_{\hat{u}}^{\text{int}}}{\partial \hat{\mathbf{u}}} = \bigcup_{e=1}^{n_{\text{elm}}} \left[\int_{\Omega} (\mathbf{R}^{\text{enr}})^T(\mathbf{x}) \mathbb{H}\mathbf{R}(\mathbf{x}) \, d\Omega \right]^e, \quad (\text{C1c})$$

$$\mathbf{K}_{\hat{u}\hat{u}}^{\Omega} = \frac{\partial \mathbf{f}_{\hat{u}}^{\text{int}}}{\partial \hat{\mathbf{u}}} = \bigcup_{e=1}^{n_{\text{elm}}} \left[\int_{\Omega} (\mathbf{R}^{\text{enr}})^T(\mathbf{x}) \mathbb{H}\mathbf{R}^{\text{enr}}(\mathbf{x}) \, d\Omega \right]^e, \quad (\text{C1d})$$

with $\mathbf{x}^* \in \tau^{\text{Col}} \subset \Omega$ and $x \in \Omega$. For the internal boundary Γ_d

$$\mathbf{K}_{\hat{u}\hat{u}}^{\Gamma_d} = \frac{\partial \mathbf{f}_{\hat{u}}^{\text{int}}}{\partial \hat{\mathbf{u}}} = \bigcup_{e=1}^{n_{\text{elm}}} \left[2 \int_{\Gamma_d} \left(\mathbf{R}^T \mathbf{n}_{\Gamma_d}^T \mathbb{D}\mathbf{R}(\mathbf{x}) - \mathbf{R}^T \frac{\partial \mathbf{t}_d}{\partial \hat{\mathbf{u}}} \right) d\Gamma \right]^e. \quad (\text{C2})$$

The tangent matrices for Γ_t yield

$$\mathbf{K}_{\hat{u}\hat{u}}^{\Gamma_t} = \frac{\partial \mathbf{f}_{\hat{u}}^{\text{int}}}{\partial \hat{\mathbf{u}}} = \bigcup_{e=1}^{n_{\text{elm}}} \left[\int_{\Gamma_t} \mathbf{R}^T \mathbf{n}_{\Gamma_d}^T \mathbb{D}\mathbf{R}(\mathbf{x}) \, d\Gamma + \mathbf{n}_{\Gamma_d}^T \mathbb{D}\mathbf{R}(\mathbf{x}^*) \right]^e, \quad (\text{C3a})$$

$$\mathbf{K}_{\hat{u}\hat{u}}^{\Gamma_t} = \frac{\partial \mathbf{f}_{\hat{u}}^{\text{int}}}{\partial \hat{\mathbf{u}}} = \bigcup_{e=1}^{n_{\text{elm}}} \left[\int_{\Gamma_t} \mathbf{R}^T \mathbf{n}_{\Gamma_d}^T \mathbb{D}\mathbf{R}^{\text{enr}}(\mathbf{x}) \, d\Gamma \right]^e, \quad (\text{C3b})$$

$$\mathbf{K}_{\hat{u}\hat{u}}^{\Gamma_t} = \frac{\partial \mathbf{f}_{\hat{u}}^{\text{int}}}{\partial \hat{\mathbf{u}}} = \bigcup_{e=1}^{n_{\text{elm}}} \left[\int_{\Gamma_t} (\mathbf{R}^{\text{enr}})^T(\mathbf{x}) \mathbf{n}_{\Gamma_d}^T \mathbb{D}\mathbf{R}(\mathbf{x}) \, d\Gamma \right]^e, \quad (\text{C3c})$$

$$\mathbf{K}_{\hat{u}\hat{u}}^{\Gamma_t} = \frac{\partial \mathbf{f}_{\hat{u}}^{\text{int}}}{\partial \hat{\mathbf{u}}} = \bigcup_{e=1}^{n_{\text{elm}}} \left[\int_{\Gamma_t} (\mathbf{R}^{\text{enr}})^T(\mathbf{x}) \mathbf{n}_{\Gamma_d}^T \mathbb{D}\mathbf{R}^{\text{enr}}(\mathbf{x}) \, d\Gamma \right]^e. \quad (\text{C3d})$$

with $\mathbf{x}^* \in \tau^{\text{Col}} \subset \Gamma_t$ and $x \in \Gamma_t$.